Supplementary

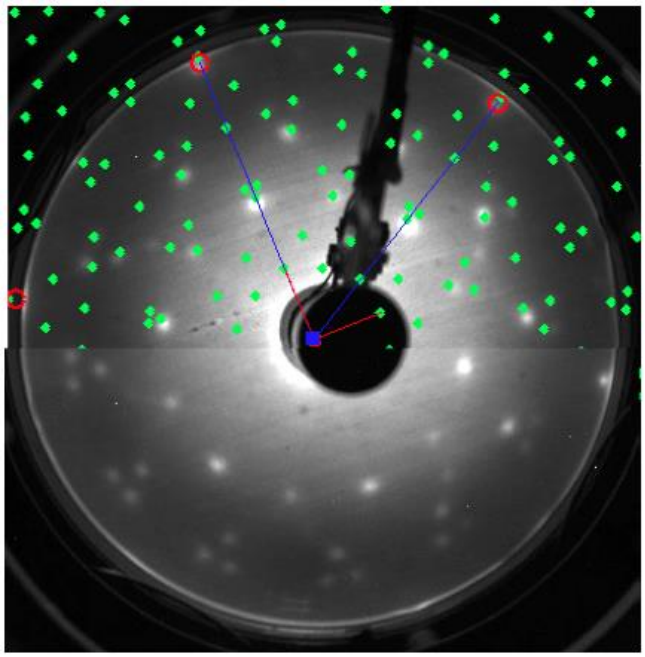

Supplementary Figure 1

Analysis of the low energy electron diffraction pattern of the X-phase. The low energy electron diffraction (LEED) pattern of the so-called X phase in the main text is superimposed with the positions of simulated diffraction spots (red and green colored circles, represent the substrate and superstructure spots, respectively). The best agreement between experiment and simulation was achieved for the superstructure matrix $\begin{bmatrix} 3.58 & 0 \\ 1.96 & 3.92 \end{bmatrix}$. The corresponding adsorbate structure shows a rectangular lattice. It may be noted that our LEED analysis indicates that the Sn atoms are likely to grow in a rectangular lattice and thus appear to adopt the body-centered-tetragonal structure of the bulk Sn phase.

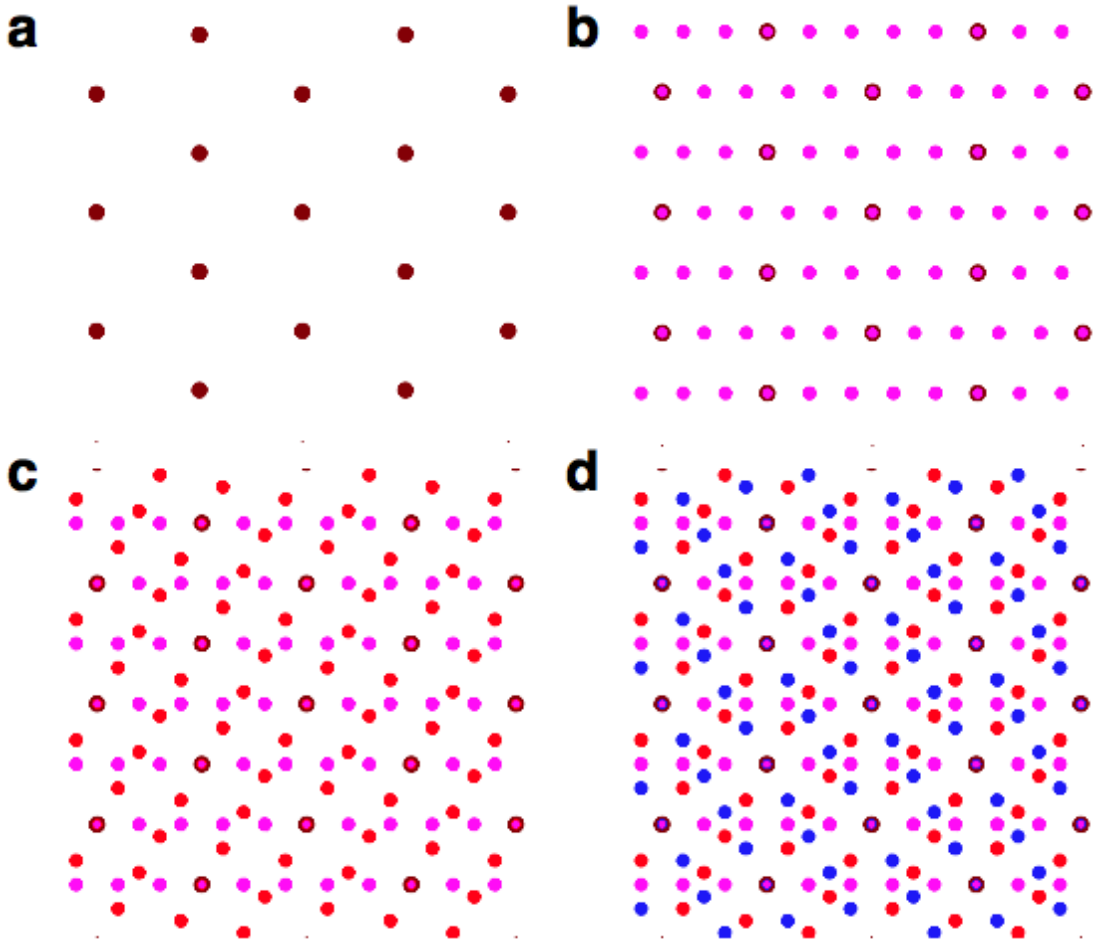

Supplementary Figure 2

Simulated diffraction pattern for the $\sqrt{7}$ **phase**. (a) Calculated low energy electron diffraction (LEED) pattern of the non-reconstructed Au(111) surface. The Au(111) substrate pattern is overlaid with a (b) single domain, (c) two domains, and (d) all three domains of the $\sqrt{7}$ Sn/Au(111) superstructure. The experimentally observed LEED pattern corresponds best to the pattern shown in (d) indicating the formation of all rotational and mirror domains of the Sn superstructure as expected from the p3m1 symmetry of the Au(111) surface. The fast Fourier transform (FFT) of scanning tunnelling microscopy (STM) image shown in the main part of the manuscript shows a perfect quantitative agreement with the simulated LEED pattern shown here in (b). This underlines the fact that our STM study was performed on a single domain of the Sn superstructure.

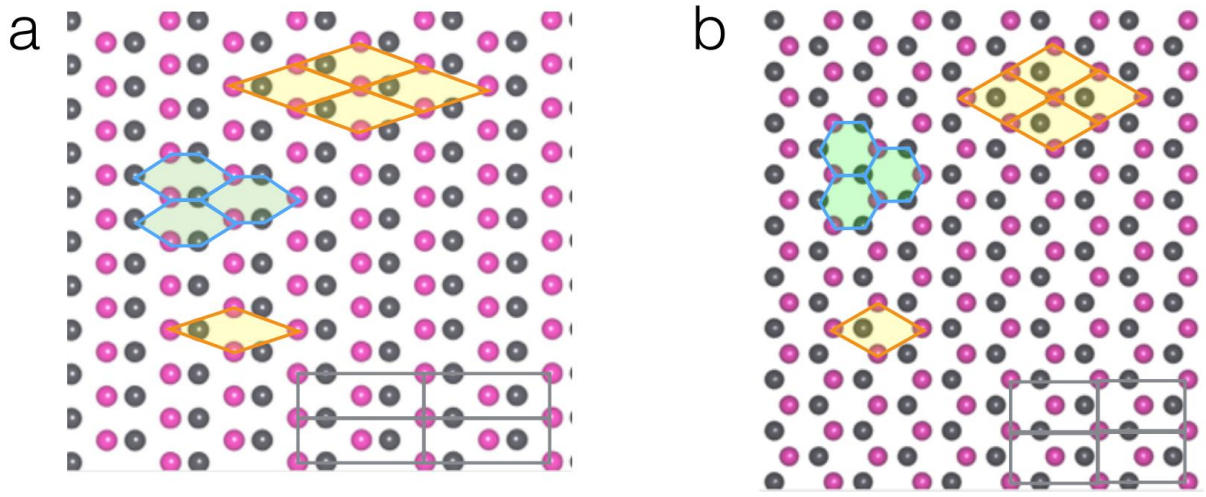

Supplementary Figure 3

Comparison of the atomic structure of $\sqrt{7}$ **phase of Sn/Au(111) with free-standing planar graphene**. (a) Atomic structure of the $\sqrt{7}$ Sn/Au(111) superstructure determined by our low energy electron diffraction (LEED) and scanning tunnelling microscopy (STM) study. (b) Atomic structure of a free-standing planar graphene film for comparison. The vertical buckling of the atoms is neglected here for simplicity. In both panels (a) and (b), the two atomic basis is represented by two atoms with different colours. The different possible unit cells are indicated by yellow rhombus and grey rectangles. The stretched and regular honeycomb is marked in sky blue. A direct comparison of all these structures shows that the $\sqrt{7}$ Sn/Au(111) superstructure can be understood as an unidirectional stretched honeycomb structure.

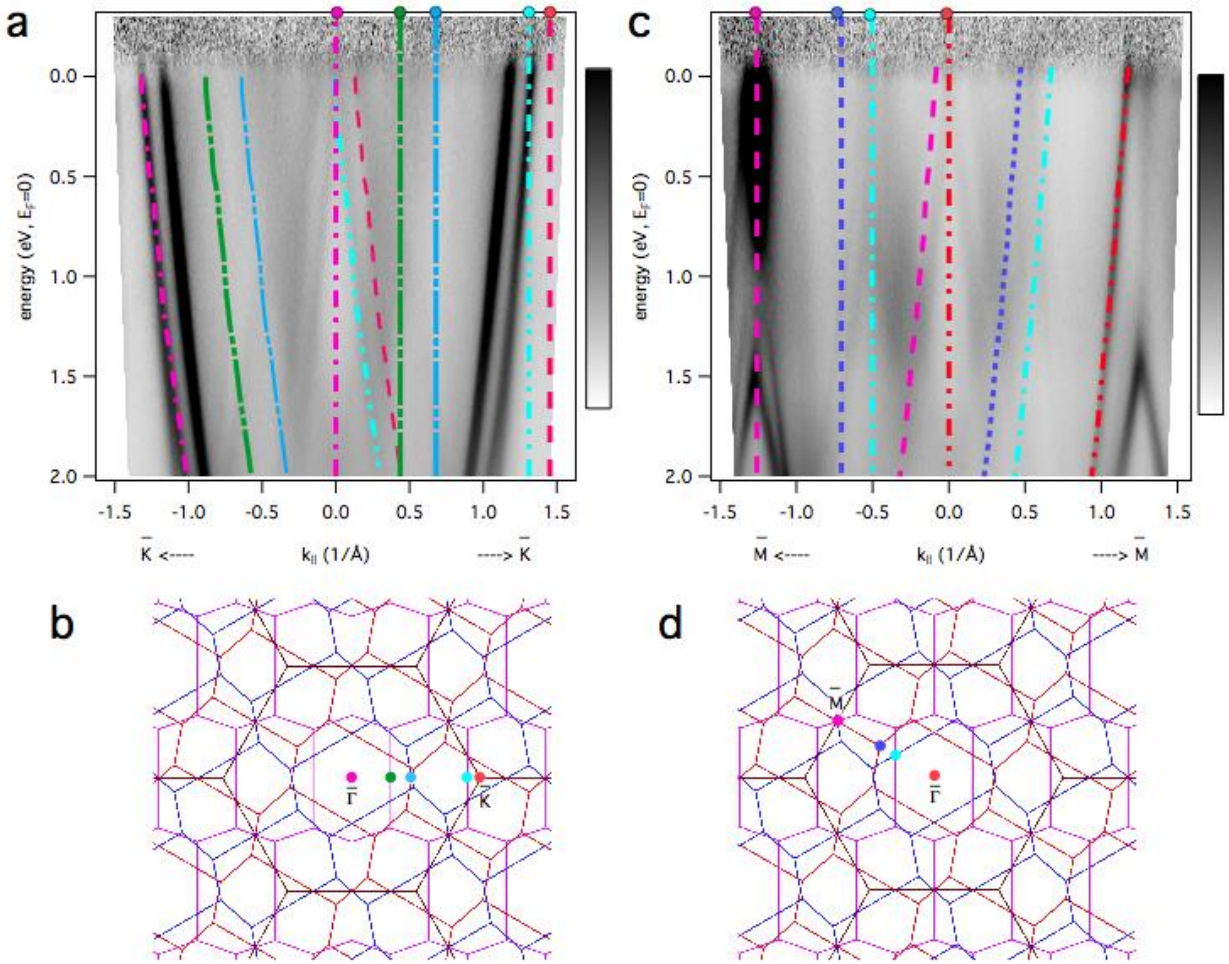

Supplementary Figure 4

Angle-resolved photoemission spectroscopy (ARPES) maps and the corresponding Brillouin zone schemes of the $\sqrt{7}$ superstructure. (a), (c) show the experimentally measured *angle-resolved photoemission spectroscopy (ARPES)* data along the high symmetry directions $\overline{\Gamma K}$ and $\overline{\Gamma M}$, respectively. (b), (d) shown the corresponding Brillouin zones of unreconstructed Au(111) (brown color) and of all three rotationally equivalent domains of the $\sqrt{7}$ superstructure of the Sn atoms on the Au(111) surface (pink, red, and blue colors). The momentum space positions of characteristic high symmetry points in the $\sqrt{7}$ Sn Brillouin zone are marked by colored dots in (b) and (d), the corresponding momentum space positions in the ARPES data are marked by vertical lines of equal color [(a) and (c)].

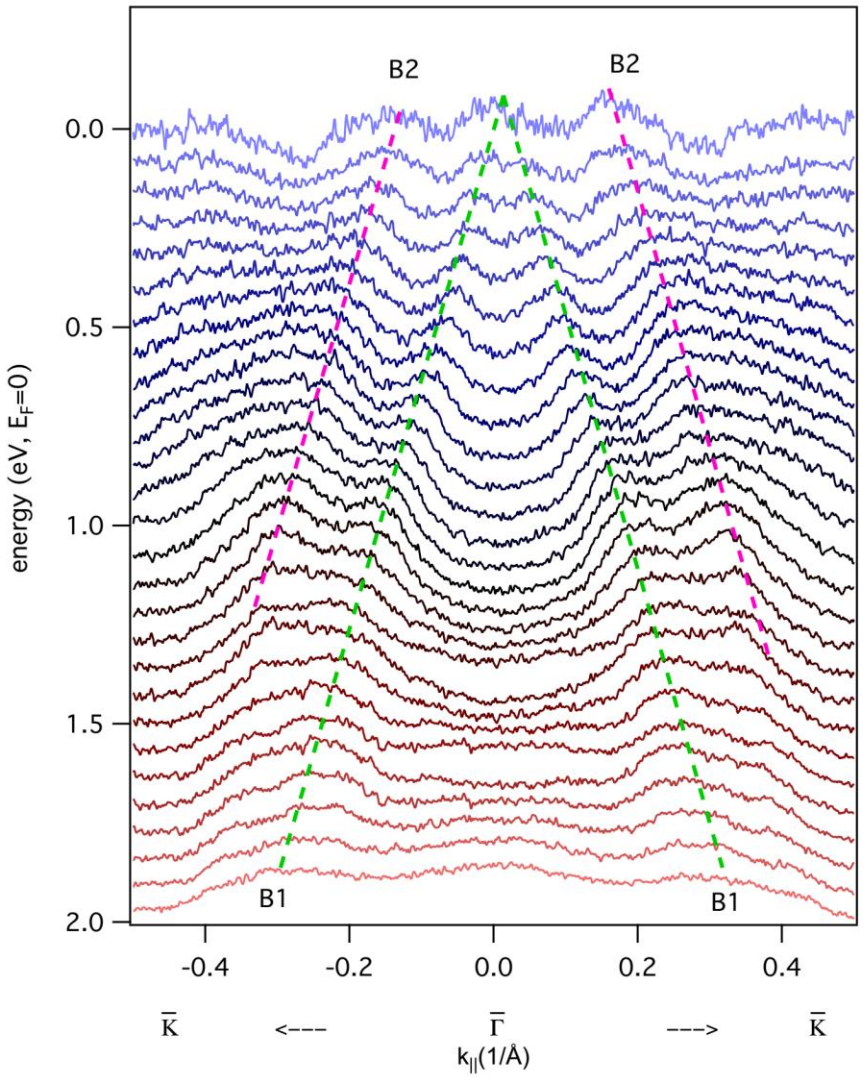

Supplementary Figure 5

Waterfall plot of angle-resolved photoemission spectroscopy (ARPES) data shown in Fig. 3b of the main manuscript. The waterfall plot clearly reveals the presence of the bands B1 and B2. Each momentum distribution curve was obtained by adding up ARPES intensity in an energy window of 50±10 meV around the center energy. All these lines are guided to eye. We would like to point out that B2 has a larger width in momentum space than B1.

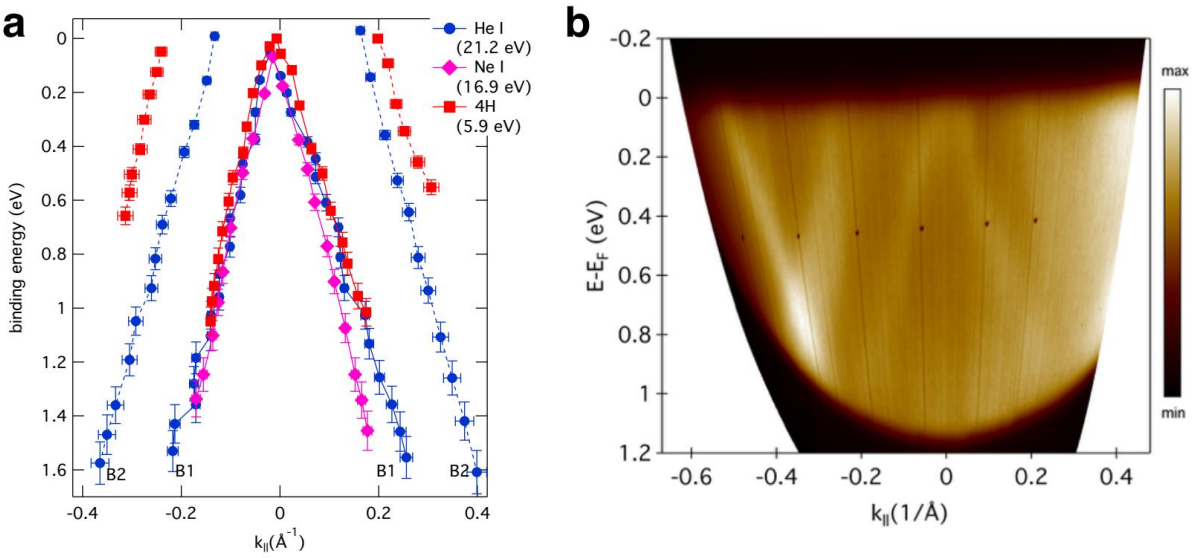

Supplementary Figure 6

Photon-energy dependent band dispersion of the band B1 and B2. (a) E($k_{||}$) plot for the inner (B1) and outer (B2) branches of the bands with similar labels as in Fig. 3b of the main text. For measurement and analysis, both the He I (21.2 eV) and Ne I (16.9 eV) lines (non-monochromatized) from a discharge lamp were used. The 5.9 eV UV measurement was carried out using the fourth harmonic of a mode-locked narrow-bandwidth Ti:sapphire laser system. All the data points were extracted by visible inspection because of the weak intensity of the spectral feature in the ARPES map. The error bar in (a) is ±5 % of the original value. The 5.9 eV photoemission was carried out with 5 V sample biasing because of very low kinetic energy of <2 eV. Thus, measured spectra has finite distortion due to bias induced electron trajectory changes, which are corrected by considering simplest mode as discussed by Hengsberger *et al*[1]. While the dispersion of band B1 is identical for all photon energies, band B2 reveals a visible difference for different photon energies. It should be noted here that band B2 appears at the edge of photoemission horizon (b). Its intensity thus becomes smeared out resulting in a larger uncertainty of the experimentally obtained dispersion of B2 for small photon energies. Thus, with the argument based on Supplementary Figure 7, we assign the origin of the band B2 to a modified valence band of Au substrate.

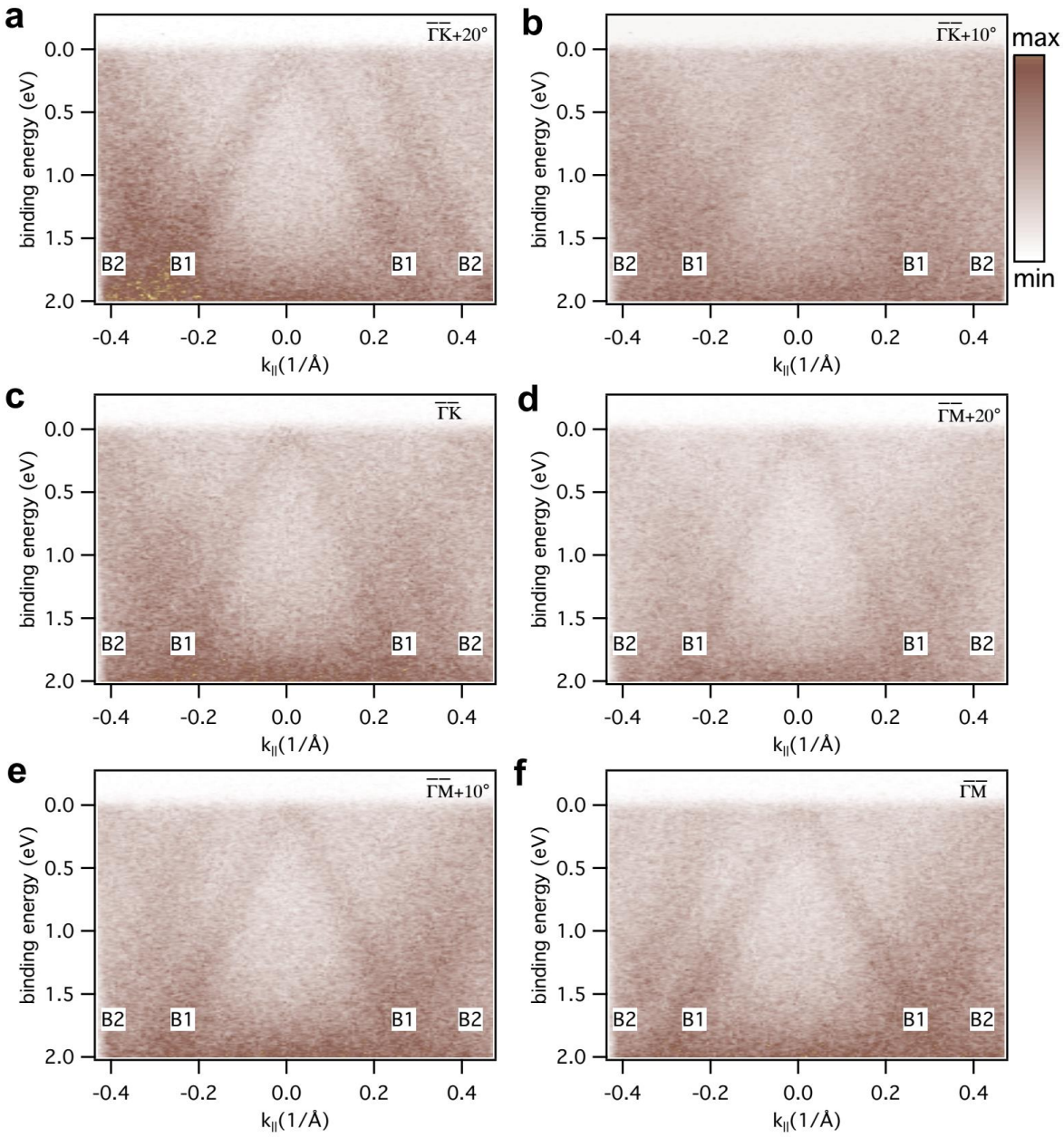

Supplementary Figure 7

Photoemission maps around the $\overline{\Gamma}$-point. Angle resolved photoemission intensity map of $\sqrt{7}$ phase of Sn/Au(111) superstructure, measured using the He I_α emission line from the discharge lamp. The intensity maps show a magnified view of the bands B1 and B2 around the $\overline{\Gamma}$ point for various azimuthal angles of the sample.

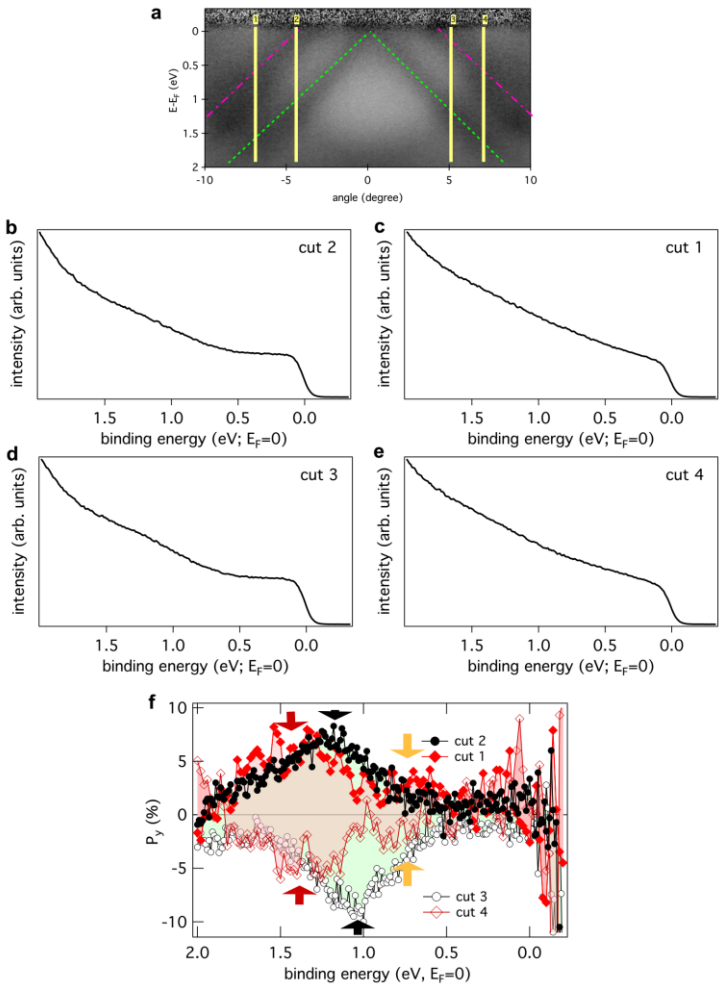

Supplementary Figure 8

Simulation of the spectral broadening of B1 and B2 in the spin-resolved photoemission data due to a lower angular resolution of the spin- and angle-resolved photoemission spectroscopy (SR-ARPES) experiment. Spin integrated spectra extracted from the (a) conventional *angle-resolved photoemission spectroscopy* (ARPES) data as shown in (b, c, d, e), at emission angles of -7°±1.5° (cut 1), -4°±1.5° (cut 2), 5°±1.5° (cut 3) and 7°±1.5° (cut 4). The spectra were averaged over an angular range of 3° which reflects the angular resolution of our spin-resolved photoemission experiment. These simulations confirm that the lack of any visible dispersion of the bands B1 and B2 in the spin-resolved photoemission spectra shown in the main text is a direct consequence of the lower angular resolution of the spin-resolved photoemission experiment. However, when all spin-polarization curves of all four energy distribution curves (EDC) cuts are overlaid as shown in (f), we see that the spin-polarization curves clearly resemble the dispersion of the band B1. Black- and red-colored arrows indicate the approximate maximum intensity position for band B1 for emission angles of 4°±1.5° and 7°±1.5°, respectively. It is readily visible that there is an energy position shift of about 200 to 300 meV between these two emission angles confirming the dispersion of band B1. The spin polarization originating from band B2 is indicated by the yellow-colored arrows. The error bar in (f) corresponds to the standard deviation of the respective measurements.

Supplementary Note 1

Possible origin of the band B2 shown in Fig. 3b of the main manuscript.

As discussed in the main text of our manuscript, the most likely explanation for B2 is that it originates from *sp*-bands of the substrate Au that are back folded (scattered) at the long range ordered Sn superstructure at the surface. In Supplementary Figure 4a, 4c, the dispersion of the substrate *sp*-bulk bands are shown by violet and red dash-dotted lines which are superimposed onto the angle-resolved photoemission spectroscopy (ARPES) data for both $\overline{\Gamma K}$ and $\overline{\Gamma M}$ high symmetry directions. The back-folding of these bands is modeled by a rigid shift of the original bands in momentum space according to characteristic distances in momentum space which correspond to crossing points in the Brillouin zones of the $\sqrt{7}$ Sn superstructure, shown as colored dots in Supplementary Figure 4b, 4d. The dispersion of the shifted bands is again superimposed on the ARPES data in Supplementary Figure 4a, 4c as dash-dotted lines. The color indicates the crossing points of the $\sqrt{7}$ phase of Sn/Au(111) Brillouin zones, which is responsible for the momentum space shift. We find that back-folding of the Au bulk *sp*-band can reasonably describe the dispersion of B2 for both $\overline{\Gamma K}$ and $\overline{\Gamma M}$ high symmetry directions, but not of B1. Therefore, we conclude that the band B2 possibly originates or had contribution from a back folding of Au *sp* bulk band.

The same analysis also allows us to exclude that B1 is caused by back folding of a *sp*-bulk band of Au. A rigid shift of the original *sp*-bulk band of Au could lead to a finite signal in the momentum and energy range of B1 in $\overline{\Gamma K}$ direction (cyan line in Supplementary Figure 4a), but not in $\overline{\Gamma M}$ direction (Supplementary Figure 4c). This different behavior in both high symmetry directions should result in an intensity modulation of B1 in a k_x-k_y cut through our ARPES data for constant binding energies. However, as discussed in our main article and shown in Fig. 3c-e, B1 exhibits an almost homogeneous intensity distribution in k_x-k_y cuts through our ARPES data. Therefore, we can conclude that back-folding of substrate bands can only explain the origin of B2, but not of B1.

Supplementary Movie 1

The movie attached as supplementary video material shows the structural phase changes upon post-deposition annealing the 0.6 monolayer of Sn on the Au(111) surface. This video was obtained from a stack of several low energy electron diffraction (LEED) pattern images acquired during the post deposition annealing at fixed electron incident energy of 40 eV. At room temperature (at the start of the movie), the diffraction pattern of the X-phase can be observed (#1 to 60). When the post-deposition annealing temperature increases, a gradual change from X-phase to the diffraction pattern of intermediate structures takes place (#300 to 420). At higher temperatures, the series of diffraction patterns passes through the $\sqrt{7}$ phase, around #570 and finally stabilizes at the $\sqrt{3}$ phase (above #990). Each of the superstructures can be stabilized at room temperature when post-deposition annealing is terminated. All phase transitions are sensitive to the annealing process and thus a careful control of the temperature is needed to stabilize each superstructure in its pure form.

Supplementary References

1. Hengsberger, M., Baumberger, F., Neff, H. J., Greber, T. & Osterwalder, J. Photoemission momentum mapping and wave function analysis of surface and bulk states on flat Cu(111) and stepped Cu(443) surfaces: A two-photon photoemission study. *Phys. Rev. B* **77,** 085425 (2008).